Frictional Contact of Soft Polymeric Shells

Riad Sahli,[1] Jeppe Mikkelsen,[1] Mathias Sätherström Boye,[1] Marcelo A. Dias,[2,*] and Ramin Aghababaei[1,†]
[1]*Department of Mechanical and Production Engineering, Aarhus University, Aarhus, Denmark*
[2]*Institute for Infrastructure and Environment, School of Engineering, The University of Edinburgh,*
EH9 3FG Edinburgh, United Kingdom

(Received 26 January 2024; accepted 19 July 2024; published 4 September 2024)

The classical Hertzian contact model establishes a monotonic correlation between contact force and area. Here, we showed that the interplay between local friction and structural instability can deliberately lead to unconventional contact behavior when a soft elastic shell comes into contact with a flat surface. The deviation from Hertzian solution first arises from bending within the contact area, followed by the second transition induced by buckling, resulting in a notable decrease in the contact area despite increased contact force. Additionally, our results invalidated a previous claim of a linear relation between friction and dissipated energy, demonstrating the suppression of both buckling and dissipation at high friction levels. Different contact regimes are discussed in terms of rolling and sliding mechanisms, providing insights for tailoring contact behaviors in soft shells.

DOI: 10.1103/PhysRevLett.133.106202

The contact area and pressure distribution between solid surfaces directly influence the frictional [1,2] and thermal resistance [3] as well as the sealing capacity [4] of the interface. Assuming a parabolic pressure profile, infinitesimal deformation, and material homogeneity, Hertzian theory [5] establishes a power-law relationship between the normal load and contact area for a wide range of elastic geometries, including spherical, cylindrical, and elliptical contacts [6] (also see Fig. 1). Alternatively, it is shown that the contact area increases linearly with the normal load when plastic deformation occurs [1]. Since these findings, the contact area-load relation has faced a transformative modification as the interplay of other factors such as friction [7–9], adhesion [10–12], roughness [13–16], and material and geometric nonlinearities [17–19] were examined. It is well established that the contact area grows with the normal load [20], while material properties, contact geometry, and surface conditions dictate the growth rate [21–25].

Recent studies [26,27] have discussed the possibilities of modifying friction laws (i.e., the correlation between the normal and frictional forces) by designing metainterfaces with certain roughness morphology. Studying the contact response of soft polymeric shells has offered another angle to modify the contact laws using the structural instability at the contact. Pauchard and Rica demonstrated a subcritical bifurcation, namely, a first-order phase transition, changes the nature of the mechanical response in contact [28]. It was observed that a flat contact exists initially between the rigid plane and the shell. However, it transitions to a postbuckling state characterized by contact along an axisymmetric circular ridge formed between the rigid plane and the inverted shell. The relevant parameters of this problem are material, a shell's Young's modulus E, and geometrical, a shell's radius R and thickness h. The combination of these results into the relevant force scale, $F_0 \equiv Eh^3/R$, and a detailed analysis proposes three regimes [29]: (i) Hertzian regime with a circular contact area, for a range of forces $F \ll F_0$, where deformation occurs within a region smaller than the shell thickness, h; (ii) intermediate regime, where

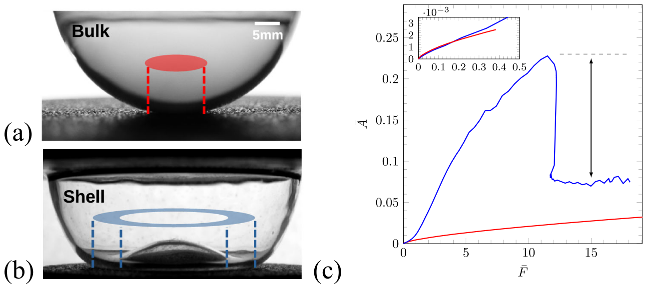

FIG. 1. (a) Bulk hemisphere of PDMS in dry contact with a PLA plate. The contact area is circular and increases with normal load, following the Hertzian solution, as illustrated by the red line in panel (c). (b) PDMS hemispherical shell in dry contact with a PLA plate, as shown by the solid blue line in panel (c). (c) This panel presents the variation of the normalized contact area $[\bar{A} = 2A/(\pi R^2)]$ as a function of the normalized normal load $[\bar{F} = FR/(Eh^3)]$ for both the bulk hemisphere and the shell. The graph highlights unconventional contact behavior where the contact area decreases (marked by a double arrow) and stabilizes despite an increase in the normal load.

---

[*] Contact author: Marcelo.Dias@ed.ac.uk

[†] Contact author: ra@mpe.au.dk

$F \sim F_0$ and equilibrium is obtained by a balance between bending and stretching, the shell flattens in a manner assumed to be similar to Hertzian contact with a disklike contact area; (iii) the postbuckling regimes, where $F > F_0$ and the stretching energy caused by sphere flattening becomes significant, the shell destabilizes and undergoes mirror buckling, transitioning into an inverted shape [30]. This behavior is akin to the isometric problem described by Pogorelov [31]. Recent studies [32–34] have demonstrated secondary buckling instability, where a transition from the axisymmetric to asymmetric deformation mode with multiple vertices occurs at large indentation [33]. The critical role of structural imperfections [35] and adhesion [36–38] on shell buckling has also been explored. Despite these advances in understanding the mechanics of shell indentation, there still exist limitations in the exploration of the effect of structural instability and friction on contact morphology and pressure distribution.

In this Letter, we examine the evolution of contact morphology and pressure when a thin shell comes into contact with a rigid and flat surface within the axisymmetric deformation regime. Our experiments and numerical simulations show that a circular contact area is first established and grows by indentation, followed by a smooth transition from circular to disklike contact as a result of bending. As indentation progresses, a secondary transition occurs, resulting in a sharp reduction in the contact area despite increased contact force. Our results led to three novel discoveries: (1) the force-contact area deviates from Hertzian solution in the intermediate regime, where the contact geometry transitions from circular (Fig. 3—p_0) to disklike contact (Fig. 3—p_1); (2) a nonmonotonic force-contact area relation can be achieved in connection with the shell instability (postbuckling regime), which is dictated by the local friction; and (3) friction introduces hysteresis upon unloading with a maximum at a critical coefficient of friction (CoF), after which hysteresis drops as high friction suppresses sliding. The critical aspect of our findings, which pertains to the contact behavior in the intermediate regime, is that we observed a departure from previous claims that full contact is maintained until the bifurcation point [29]. Additionally, it is also shown that local friction delays and eventually suppresses the postbifurcation regime, hindering the abrupt change in the force-contact area relation and hysteresis.

The snapshots in Figs. 1(a) and 1(b) showcase the deformation modes of a bulk solid and a shell, both made from cross-linked polydimethylsiloxane (PDMS), upon contact with a flat polylactic acid (PLA) plate. Figure 1(c) presents the force-contact area relation, highlighting an early deviation from Hertzian solution, followed by a sudden drop in the contact area when a transition occurs in the deformation mode. First, we experimentally study the contact of a thin, elastic hemispherical shell made of cross-linked PDMS [40] with a flat PLA plate, having a roughness of $Sa = 15$ μm to suppress the contribution of adhesion (Fig. 1). Systematic investigation of adhesion is not performed in this study, due to the difficulty of varying adhesion and friction independently. The PDMS shell, with a radius of $R = 25$ mm and thickness $h = 1.33 \pm 0.06$ mm, is made by pouring a PDMS mixture over a 25 mm radius bearing ball [41]. In a displacement-control manner (see Supplemental Fig. S1 [39]), the PLA plate comes into contact with the shell at a constant velocity of 10 mm/ min, where the force-displacement data are recorded. A side camera is used to monitor the deformation of the shell. To study the effect of the friction coefficient, we ran the test under dry and lubricated conditions, where Kema GL-68 is used as the lubricant. Additional experiments are conducted to measure μ between PDMS and PLA under dry (1.0 ± 0.2) and lubricated (0.48 ± 0.09) contacts (see Supplemental Figs. S2 and S3 [39]).

To complement our experiments with details of contact area and pressure evolution over a wider range of μ, we performed systematic finite element simulations using the commercial software ABAQUS [42]. A fixed boundary condition is applied at the top, while a displacement is applied to the plate (Supplemental Fig. S4 [39]). The shell mesh is presented in Supplemental Fig. S5. Details of loading and boundary conditions as well as material properties are presented in the Supplemental Material [39].

Figure 2(a) summarizes the experimental and numerical results, presenting the evolution of contact force [$\bar{F} = FR/(Eh^3)$] during the loading and unloading stages under dry ($\mu = 1.0$) and lubricated ($\mu = 0.48$) conditions. We additionally include simulation results for the frictionless ($\mu = 0.0$) and high-friction ($\mu = 2.2$) scenarios. Despite the absence of the adhesion effect in our simulation, a close agreement between the experimental and numerical results has been obtained for the dry and lubricated contacts in all stages of indentation. As seen, the contact force monotonically increases with the indentation until buckling occurs, after which a small drop is identified in the indentation force. The force continues to increase at a lower rate in the postbuckling regime. One can see that the evolution of force in the postbuckling regime is a function of the CoF. As friction rises, it opposes the compressive stresses within the shell, increasing the critical force needed for instability initiation. In other words, the heightened frictional forces hinder relative motion between surfaces, strengthening resistance to compressive loading. Consequently, the critical force threshold rises due to the combined effects of friction-induced resistance and the reaction to compressive stresses on the shell material. This observation highlights how frictional mechanics control the structural stability of materials.

A significant dissipation through hysteresis is also observed upon unloading in both cases. It is evident that as the CoF increases, the buckling is delayed, while a larger energy dissipation occurs upon unloading. As expected, no dissipation occurs in the frictionless case, indicating that sliding in the postbuckling stage is the main source of energy dissipation. Interestingly, it can be seen that a high

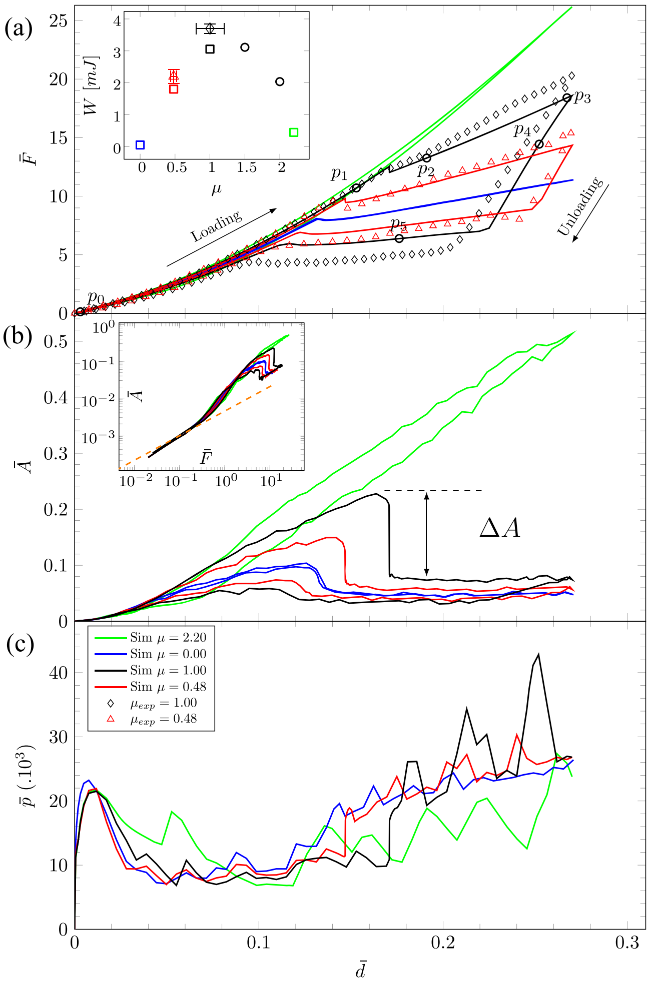

FIG. 2. The evolutions of normalized force $\bar{F}$, contact area $\bar{A}$, and maximum contact pressure $\bar{p} = P_{\max}/E$ (times 10^3), as a function of the indentation ratio $\bar{d} = d/R$ are presented for different CoFs. Experimental results are displayed using black diamond symbols for dry conditions and red triangle symbols for lubricated conditions across all panels. Simulations are depicted with solid lines for various CoFs: $\mu = 0$ (blue), $\mu = 0.48$ (red), $\mu = 1.0$ (black), and $\mu = 2.2$ (green). Insets include the dissipated energy during unloading W presented in panel (a), highlighting a parabolic correlation with a CoF, and two key transitional points in panel (b): the deviation of the force-area relation from the Hertzian solution (orange dash line) due to bending and a sudden drop in contact area due to shell buckling. The deviation from Hertzian can also be seen from the pressure drop in (c).

CoF can completely avoid shell buckling and, consequently, energy dissipation is reduced to a minimum. The inset of Fig. 2(a) shows a parabolic relation between the dissipated energy ($W = \oint_S F dx$) and CoF, indicating the existence of a critical CoF, where sliding and dissipation in the postbuckling stage are maximized (also see Supplemental Table S1 [39]). This critical CoF may be a function of geometrical (thickness, diameter) and material parameters (Young modulus).

The evolution of the contact area in different stages of indentation is presented in Fig. 2(b). It can be seen that the normalized contact area [$\bar{A} = 2A/(\pi R^2)$] increases monotonically until the point of instability, after which a sharp reduction occurs (also see Supplemental Table S1 [39]). For the case of high friction ($\mu = 2.2$) and the absence of instability, the contact area increases for the entire simulation. The inset figure in Fig. 2(b), compares the force-contact area relationship with the Hertzian solution shown by an orange dashed line in the loading regime. Interestingly, it can be seen that deviation from the Hertzian solution occurs in the intermediate regime and before the point of buckling. This observation challenges the previous assumption of Hertzian-like behavior in the intermediate regime [29]. Remarkably, the contact area remains constant in the postbuckling regime despite the increase in the indentation force. This stands in contrast to the contact response of a bulk sphere, where the contact area monotonically grows [5,21] (also see Fig. 1). Three regimes of deformation can also be distinguished by monitoring the average contact pressure as a function of indentation. The maximum contact pressure $P_{\max}$ is defined as maximum values of the pressure $p(x)$ in the pressure field at a given indentation $\bar{d}$. Figure 2(c) presents the maximum contact pressure normalized by the elastic modulus ($\bar{p} = P_{\max}/E$). The pressure initially increases in the Hertzian regime (regime I), followed by a smooth drop and saturation (regime II). Clearly, it can be seen that the pressure in the intermediate regime II does not follow the Hertzian behavior shown in regime I. The maximum pressure experiences a sharp increase as a result of buckling and the reduction in the contact area [see Fig. 2(b)], indicating the transition into the postbuckling regime III.

An *in situ* analysis of shell deformation and the evolution of contact area and pressure for the dry contact scenario ($\mu = 1.0$), corresponding to marked points p_0–p_5 in Fig. 2(a), is illustrated in Fig. 3 (see Supplemental Movies [39] for other CoFs). It can be seen that the numerical simulations predict the profile of the shell in all regimes. At the onset of contact (p_0), the circular contact geometry [Fig. 3(b)] and the parabolic contact pressure distribution [Fig. 3(c)] follow the Hertzian solution. p_1 demonstrates the deviation from the Hertzian solution in the intermediate regime but before the point of buckling by showing a disklike contact area and nonparabolic pressure distribution as a direct result of bending in the shell. A similar pressure profile has also been derived theoretically [43]. Contrary to the parabolic Hertzian pressure distribution, the pressure in the intermediate regime reduces from the leading edge to the trailing edge (see Supplemental Movies [39]), indicating that the change in the contact morphology is dominated by the rolling mechanism. This explains the minimization of dissipation until the point of buckling, after which sliding and thus dissipation occur at the contact. In the postbuckling regime (p_2 and p_3), the

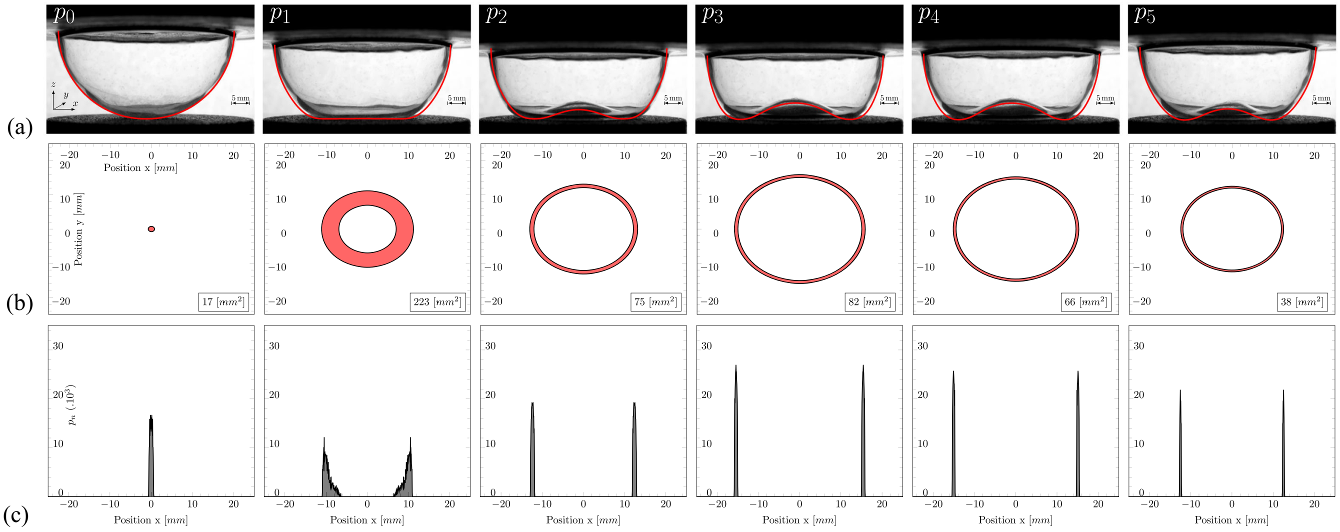

FIG. 3. (a) *In situ* snapshots of a shell profile indented by a PLA plate, under dry contact ($\mu = 1.0$) at different stages of indentation, corresponding to points p_0–p_5, marked in Fig. 2(a). The profiles obtained from the simulation are superimposed with red solid lines for comparison. (b) and (c) present, respectively, the corresponding contact morphology and the contact pressure distribution $[p(x)/E]$, obtained from simulations multiplied by 10^3 for clarity. Inset numbers in (b) present the total contact area. The evolution of contact area and pressure distribution, as well as the indentation force and shell profile for different CoFs can be seen in Supplemental Movies [39].

contact occurs along a circular ridge with a parabolic pressure distribution across the contact width. In the unloading phase, the outer side of the shell is first unloaded elastically (p_4) as shown in Supplemental Fig. S6. In this regime, while the buckled (inner) side of the shell remains fairly stationary due to friction (see Supplemental Fig. S7a), the outer side unrolls, causing a reduction in the contact area (Supplemental Fig. S7b). The unloading phase continues with a transition, where the local tangential load overcomes friction. In this regime (p_5), while the contact area remains constant [see Fig. 2(b)], dissipation occurs via frictional sliding. Eventually, the shell unbuckles, after which the Hertzian solution is recovered.

Another intriguing effect of friction is that it makes the loading-unloading response asymmetric. Figure 4 demonstrates the evolution of contact morphology during the loading and unloading phases by showing the location and size of the contact area. The contact size refers to the radius of a circular contact in the Hertzian regime and the width of the annular contact area in the intermediate and postbuckling regimes. Noting the variation of contact size, three regimes of Hertzian, intermediate, and postbuckling are classified for each friction case. It can be seen that friction postpones all transition points during the loading and unloading phases, resulting in a more extended Hertzian regime during the loading, but a smaller one upon unloading. Additionally, the degree of asymmetry in the loading-unloading response increases with friction. For the high friction case ($\mu = 2.2$) where the buckling regime is absent, unloading is mainly accommodated via the rolling mechanism, explaining the absence of dissipation (also see Supplemental Movie [39]).

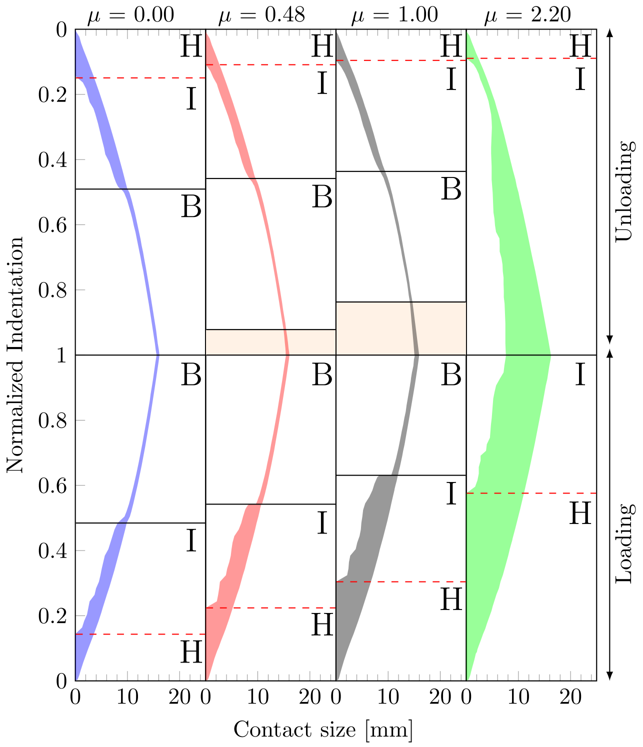

FIG. 4. The evolution of contact size and location in the loading and unloading phases for different CoFs. The indentation on the y axes is normalized by the maximum indentation. The contact size represents the radius of a circular contact in the Hertzian regime and the width of an annular contact area in the intermediate and postbuckling regimes. Letters H, I, and B denote Hertzian, intermediate, and postbuckling regimes, respectively. Red dashed lines mark the transition point between the Hertzian and intermediate regimes. The shaded areas highlight the elastic unloading at the onset of unloading for cases of $\mu = 0.48$ and 1.0.

We have shown how the interplay between structural instability and the local friction coefficient dictates the morphology of contact. It is shown that the contact behavior departs from the Hertzian solution due to bending at the onset of contact. This observation challenges the previous assumption of a Hertzian-like response in the prebuckling regime. In agreement with previous studies [29], two transition points are identified in the loading phase, classifying three regimes of deformation: Hertzian, intermediate, and postbuckling. While the contact area increases monotonically in the first two regimes, it abruptly drops and then remains constant in the postbuckling regime. The distribution of pressure in the contact zone revealed two distinct mechanisms for the evolution of the contact area: (i) the energy-preserving rolling mechanism in the Hertzian and intermediate regimes, and (ii) the dissipative frictional sliding in the postbuckling regime. In other words, the response is fully reversible (non-dissipative) in the absence of friction or the postbuckling regime. The unloading phase for $\mu = 0.48$ begins with an elastic unrolling, followed by dissipative frictional sliding. Furthermore, it is evident that friction causes a delay at all transition points, leading to the expansion and contraction of the Hertzian regime during the loading and unloading phases, respectively. The addition of adhesion in simulations would be a natural step to extend our current work, given the strong coupling between friction and adhesion, especially in the low roughness contact scenario. [36–38].

The interplay between friction, material properties, and structural instability leverages the controlled departure from Hertzian behavior and the monotonic contact force-area relation. This new understanding presents a direction to tailor the contact morphology and governing mechanism, offering solutions to a diverse range of engineering applications such as systems with superior damping capabilities [44], a sport ball [45,46], haptic robotics [47,48], or vesicle manipulation [49,50].

Acknowledgments—This research has been supported by a Marie Sklodowska-Curie Postdoctoral Fellowship under Contract No. (Proposal No. 101065669). R. A. and R. S. also acknowledge the support from the Thomas B. Thriges Fond. M. A. D. would like to thank UKRI for support under the EPSRC Open Fellowship scheme (Project No. EP/W019450/1).

---

[1] F. P. Bowden, D. Tabor, and F. Palmer, *The Friction and Lubrication of Solids* (Clarendon Press, Oxford, 1950).

[2] J. Archard, Elastic deformation and the laws of friction, Proc. R. Soc. A **243**, 190 (1957).

[3] C. V. Madhusudana and C. Madhusudana, *Thermal Contact Conductance* (Springer, New York, 1996), Vol. 79.

[4] B. N. Persson, O. Albohr, U. Tartaglino, A. Volokitin, and E. Tosatti, On the nature of surface roughness with application to contact mechanics, sealing, rubber friction and adhesion, J. Phys. Condens. Matter **17**, R1 (2004).

[5] H. Hertz, Ueber die berührung fester elastischer Körper, J. Reine Angew. Math. **1882**, 156 (1882).

[6] V. L. Popov, M. Heß, and E. Willert, *Handbook of Contact Mechanics: Exact Solutions of Axisymmetric Contact Problems* (Springer Nature, Berlin, Heidelberg, 2019).

[7] S. Carlsson, S. Biwa, and P.-L. Larsson, On frictional effects at inelastic contact between spherical bodies, Int. J. Mech. Sci. **42**, 107 (2000).

[8] B. Storåkers and D. Elaguine, Hertz contact at finite friction and arbitrary profiles, J. Mech. Phys. Solids **53**, 1422 (2005).

[9] B. Weber, J. Scheibert, M. P. de Boer, and A. Dhinojwala, Experimental insights into adhesion and friction between nominally dry rough surfaces, MRS Bull. **47**, 1237 (2022).

[10] L. Pastewka and M. O. Robbins, Contact between rough surfaces and a criterion for macroscopic adhesion, Proc. Natl. Acad. Sci. U.S.A. **111**, 3298 (2014).

[11] H. Bense, M. Tani, M. Saint-Jean, E. Reyssat, B. Roman, and J. Bico, Elastocapillary adhesion of a soft cap on a rigid sphere, Soft Matter **16**, 1961 (2020).

[12] C. Oliver, D. Dalmas, and J. Scheibert, Adhesion in soft contacts is minimum beyond a critical shear displacement, J. Mech. Phys. Solids **181**, 105445 (2023).

[13] J. A. Greenwood and J. H. Tripp, The elastic contact of rough spheres, J. Appl. Mech. **34**, 153 (1967).

[14] B. Luan and M. O. Robbins, The breakdown of continuum models for mechanical contacts, Nature (London) **435**, 929 (2005).

[15] R. Aghababaei, E. E. Brodsky, J.-F. Molinari, and S. Chandrasekar, How roughness emerges on natural and engineered surfaces, MRS Bull. **47**, 1229 (2022).

[16] M. H. Müser and L. Nicola, Modeling the surface topography dependence of friction, adhesion, and contact compliance, MRS Bull. **47**, 1221 (2022).

[17] B. Weber, T. Suhina, T. Junge, L. Pastewka, A. Brouwer, and D. Bonn, Molecular probes reveal deviations from amontons' law in multi-asperity frictional contacts, Nat. Commun. **9**, 888 (2018).

[18] C.-E. Wu, K.-H. Lin, and J.-Y. Juang, Hertzian load–displacement relation holds for spherical indentation on soft elastic solids undergoing large deformations, Tribol. Int. **97**, 71 (2016).

[19] H. Ghaednia, X. Wang, S. Saha, Y. Xu, A. Sharma, and R. L. Jackson, A review of elastic–plastic contact mechanics, Appl. Mech. Rev. **69**, 060804 (2017).

[20] J. H. Dieterich and B. D. Kilgore, Direct observation of frictional contacts: New insights for state-dependent properties, Pure Appl. Geophys. **143**, 283 (1994).

[21] R. Sahli, G. Pallares, C. Ducottet, I. Ben Ali, S. Al Akhrass, M. Guibert, and J. Scheibert, Evolution of real contact area under shear and the value of static friction of soft materials, Proc. Natl. Acad. Sci. U.S.A. **115**, 471 (2018).

[22] R. Sahli, G. Pallares, A. Papangelo, M. Ciavarella, C. Ducottet, N. Ponthus, and J. Scheibert, Shear-induced anisotropy in rough elastomer contact, Phys. Rev. Lett. **122**, 214301 (2019).

[23] A. Papangelo, J. Scheibert, R. Sahli, G. Pallares, and M. Ciavarella, Shear-induced contact area anisotropy explained

by a fracture mechanics model, Phys. Rev. E **99**, 053005 (2019).

[24] K. Matsuda, S. Mori, A. Hatanaka, T. Sunahara, and K. Nakamura, Effect of specimen thickness on growth of real contact area of rubber with two-dimensional regular wavy surface, Tribol. Int. **124**, 184 (2018).

[25] Y. Mo, K. Turner, and I. Szlufarska, Friction laws at the nanoscale, Nature (London) **457**, 1116 (2009).

[26] V. Slesarenko and L. Pastewka, The bumpy road to friction control, Science **383**, 150 (2024).

[27] A. Aymard, E. Delplanque, D. Dalmas, and J. Scheibert, Designing metainterfaces with specified friction laws, Science **383**, 200 (2024).

[28] L. Pauchard and S. Rica, Contact and compression of elastic spherical shells: The physics of a ‘ping-pong’ball, Philos. Mag. B **78**, 225 (1998).

[29] B. Audoly and Y. Pomeau, *Elasticity and Geometry: From Hair Curls to the Non-Linear Response of Shells* (Oxford University Press, New York, 2010).

[30] M. Gomez, D. E. Moulton, and D. Vella, The shallow shell approach to Pogorelov’s problem and the breakdown of ‘mirror buckling’, Proc. R. Soc. A **472**, 20150732 (2016).

[31] A. V. Pogorelov, *Bendings of Surfaces and Stability of Shells* (American Mathematical Soc., Providence, 1988), Vol. 72.

[32] A. Vaziri, Mechanics of highly deformed elastic shells, Thin-Walled Struct. **47**, 692 (2009).

[33] A. Nasto, A. Ajdari, A. Lazarus, A. Vaziri, and P. M. Reis, Localization of deformation in thin shells under indentation, Soft Matter **9**, 6796 (2013).

[34] S. Knoche and J. Kierfeld, The secondary buckling transition: Wrinkling of buckled spherical shells, Eur. Phys. J. E **37**, 1 (2014).

[35] A. Lee, F. López Jiménez, J. Marthelot, J. W. Hutchinson, and P. M. Reis, The geometric role of precisely engineered imperfections on the critical buckling load of spherical elastic shells, J. Appl. Mech. **83**, 111005 (2016).

[36] C. Zhao, K.-t. Wan, and W. Shan, Progressive adhesion mechanics of elastomeric shells against a rigid substrate: From thin to thick, Extreme Mech. Lett. **68**, 102140 (2024).

[37] C. Zhao, X. Chen, W. Shan, and K.-t. Wan, Adherence of a hyperelastic shell on a rigid planar substrate, Int. J. Solids Struct. **236**, 111351 (2022).

[38] W. Wang, J. Gray, S. Julien, and K.-T. Wan, Mechanical characterization of a convex shell (contact lens) with meridional thickness variation, Exp. Mech. **58**, 997 (2018).

[39] See Supplemental Material at http://link.aps.org/supplemental/10.1103/PhysRevLett.133.106202 for additional experimental details, simulation methods, materials characterization, and supporting figures to further substantiate our findings.

[40] J. Le Rouzic, P. Delobelle, P. Vairac, and B. Cretin, Comparison of three different scales techniques for the dynamic mechanical characterization of two polymers (pdms and su8), Eur. Phys. J. Appl. Phys. **48** (2009).

[41] A. Lee, P.-T. Brun, J. Marthelot, G. Balestra, F. Gallaire, and P. M. Reis, Fabrication of slender elastic shells by the coating of curved surfaces, Nat. Commun. **7**, 11155 (2016).

[42] G. Abaqus, Abaqus 15.50, Dassault Systemes Simulia Corporation, Providence, RI, USA, 3, 2021.

[43] D. P. Updike and A. Kalnins, Contact pressure between an elastic spherical shell and a rigid plate, J. Appl. Mech. **39**, 1110 (1972).

[44] R. Ullah, M. Vafaei, S. C. Alih, and A. Waheed, A review of buckling-restrained braced frames for seismic protection of structures, Phys. Chem. Earth A/B/C **128**, 103203 (2022).

[45] T. Rémond, V. Dolique, F. Vittoz, S. Antony, R. G. Rinaldi, L. Manin, and J.-C. Géminard, Dynamical buckling of a table-tennis ball impinging normally on a rigid target: Experimental and numerical studies, Phys. Rev. E **106**, 014207 (2022).

[46] R. G. Rinaldi, L. Manin, C. Bonnard, A. Drillon, H. Lourenco, and N. Havard, Non linearity of the ball/rubber impact in table tennis: Experiments and modeling, Procedia Eng. **147**, 348 (2016).

[47] A. M. Nasab, A. Sabzehzar, M. Tatari, C. Majidi, and W. Shan, A soft gripper with rigidity tunable elastomer strips as ligaments, Soft Rob. **4**, 411 (2017).

[48] A. Gedsun, R. Sahli, X. Meng, R. Hensel, and R. Bennewitz, Bending as key mechanism in the tactile perception of fibrillar surfaces, Adv. Mater. Interfaces **9**, 2101380 (2022).

[49] F. Quemeneur, C. Quilliet, M. Faivre, A. Viallat, and B. Pépin-Donat, Gel phase vesicles buckle into specific shapes, Phys. Rev. Lett. **108**, 108303 (2012).

[50] N. Tsapis, E. R. Dufresne, S. S. Sinha, C. S. Riera, J. W. Hutchinson, L. Mahadevan, and D. A. Weitz, Onset of buckling in drying droplets of colloidal suspensions, Phys. Rev. Lett. **94**, 018302 (2005).